Proceedings of ASME Turbo Expo 2016: Turbine Technical Conference and Exposition
GT2016
June 13-17, 2016, Seoul, South Korea

GT2016-57234

AEROACOUSTIC OPTIMIZATION OF RADIAL FANS FOR MEDICAL APPLICATIONS

Michael Stadler
Ninsight
Graz, Austria

Julien Grilliat
ebm-papst St. Georgen
St. Georgen, Germany

Wolfgang Laufer
ebm-papst St. Georgen
St. Georgen, Germany

Michael B. Schmitz
ebm-papst St. Georgen
St. Georgen, Germany

ABSTRACT

In recent years there is a growing number of patients suffering from pneumonia, chronic obstructive pulmonary disease or asthma. In these situations, the application of Continuous Positive Airway Pressure (commonly known as CPAP) is indicated by clinicians. It is a noninvasive means of healthcare used widely. As a more advanced technique, the positive airway pressure may follow a time-cycled change between two preset pressure values. This technique is known as BPAP (Bi-level Positive Airway Pressure).

The devices are used mainly during sleep at home. Hence the aeroacoustic requirements are critical. In addition the devices must be portable and compact. Furthermore, the high frequency of pressure change required in BPAP devices poses additional demands on the design. Due to the complexity of the overall design problem, it may be solved efficiently by multi objective optimization.

The pressure head in these devices is generated by radial fans. For the aerodynamic optimization, we utilize a RANS solver. For the aeroacoustic optimization we use the Lattice-Boltzmann Method (LBM). Both are operating on a parametric geometric model of the fan and housing. For the propagation of sound waves into the far-field, we develop algorithmic strategies for using the Ffowcs Williams-Hawkings (FW-H) equation with the LBM. The constrained multi objective optimization is driven by a variant of the NSGA-II algorithm.

We outline the complete optimization procedure for a BPAP device. Our numerical results are compared with physical tests. To analyze the contribution of selected geometric features to the emitted sound pressure, we perform a sensitivity study. The new algorithmic arrangement has shown to drastically cut development costs and time.

INTRODUCTION

Due to environmental pollution and associated factors, the number of patients affected by diseases of the lung is rising worldwide. In particular, for pneumonia, this can be observed in the developed world [1], but also in the developing countries (see [2] and [3] among others). The epidemiology of chronic obstructive pulmonary disease (COPD) has been studied in [4] and [5]. Furthermore, the increased prevalence of asthma over a recent period of 10 years has been documented in [6] among others.

A related clinical issue is obstructive sleep apnea (OSA) [7]. It is characterized by repetitive pauses in breathing during sleep, and is usually associated with a reduction in blood oxygen saturation and arousal from sleep. OSA is commonly accompanied with snoring.

The above mentioned diseases form the main indications for the application of Continuous Positive Airway Pressure (CPAP). It is a mode of respiratory ventilation, which reduces the apneas by delivering a stream of compressed air via a face mask, thereby splinting the airway so that unobstructed breathing becomes possible. CPAP devices were initially used at home but are now also in widespread use across intensive care units.

A more advanced technique uses time-cycled or flow-cycled change between two different levels of positive airway pressure. It generates inspiratory and expiratory pressure gradients that complement the patient's own respiratory cycle, thereby optimizing the lungs' efficiency and reducing the work of breathing. This technique is known as Bi-level Positive Airway Pressure (BPAP). Since the pressure is controlled by the rotational speed of the fan, the inertial properties of the rotor play an important role.

Studies have shown that the main disadvantage of this technique is patient related non-compliance because of noise emission or bulky devices (see [8] and [9]). Hence, during the design and improvement of new devices, these criteria should play an important role.

The optimization of fans is driven mainly by the availability of robust optimization algorithms, aeroacoustic prediction methods and large scale computing resources. These topics have

been discussed recently in the papers [10], [11] and [12] among others. In particular, evolutionary algorithms were used with the Lattice-Boltzmann Method in [13], [14] and [15] among others.

In this paper we outline the complete optimization procedure for the radial fan, which forms the central part of a BPAP device. The rotor has a diameter of $D = 46$ mm. Its main operating points are provided in Table 1. The rotational speed lies in the range between $n = 30000 - 41000\ \mathrm{min}^{-1}$.

Operating point	φ	ψ
1	0.0047	0.63
2	0.0238	0.77
3	0.0238	0.90
4	0.024	1.02

Table 1: Operating points of the fan in non-dimensional form.

For the optimization, both the spatial and the aeroacoustic requirements are considered. In order to initialize the flow field, we use a RANS solver. However, the aeroacoustic objective function is evaluated using a code based on the Lattice-Boltzmann method (LBM).

The paper is organized as follows: in the following section we outline the parameterization of the fan and housing geometry. Subsequently we discuss the optimization algorithm, thereby specifying the objective functions and constraints. The necessary simulation models are introduced in the next section. In particular, since we are interested in the sound pressure in the far field, algorithmic strategies for using the FW-H equation with LBM based aeroacoustics are developed. Different interpolation strategies for the output pressure time history from the FW-H solver are discussed. For the validation of results, we perform physical measurements. The paper concludes with an evaluation of the design improvement of the BPAP fan. In addition, the numerical efficiency of the optimization procedure is outlined.

PARAMETERIZATION OF THE FAN GEOMETRY

To facilitate an efficient optimization procedure, the parametric space is built according to the following rules:

- exclusion of physically impossible configurations, and
- minimization of the number of parameters.

The CFD model is created by using geometric templates. This allows to easily adapt the design space in order to harness further potential for optimization.

Blade. To keep production costs low, we aim to avoid complex tooling equipment. Hence, the physical rotor will be produced by a single step of injection die molding. This constrains the shape of the blade to be represented by an axial extrusion. The tip gap is specified by a constant value, which is excluded from the design space. The meridional section of the blade is defined by B-splines $\boldsymbol{B_1}(s)$ and $\boldsymbol{B_2}(s)$. Their control vertices $\boldsymbol{p_i}, i = 1 \ldots 4$ with tangent vectors $\boldsymbol{t_i}, i = 1 \ldots 4$, act as parameters. In addition, the tip geometry is defined by radius r_t. The blades are distributed in a non-equidistant way to reduce tonal noise [16] (see Fig. 1).

Volute. The flow from the rotor expands into the volute. It is designed as a rectangular profile with variable axial depth $s(\vartheta)$ and constant radius fillets r_1 and r_2. The outer radius of the profile is described in a classical way by a logarithmic spiral according to

$$r(\vartheta) = R \cdot e^{\vartheta \tan \alpha} \tag{1}$$

The transition from the volute to the exit nozzle defines the tongue, which is characterized by parameter r_3 (see Fig. 1).

To summarize, the design space is governed by the parameters presented in Table 2.

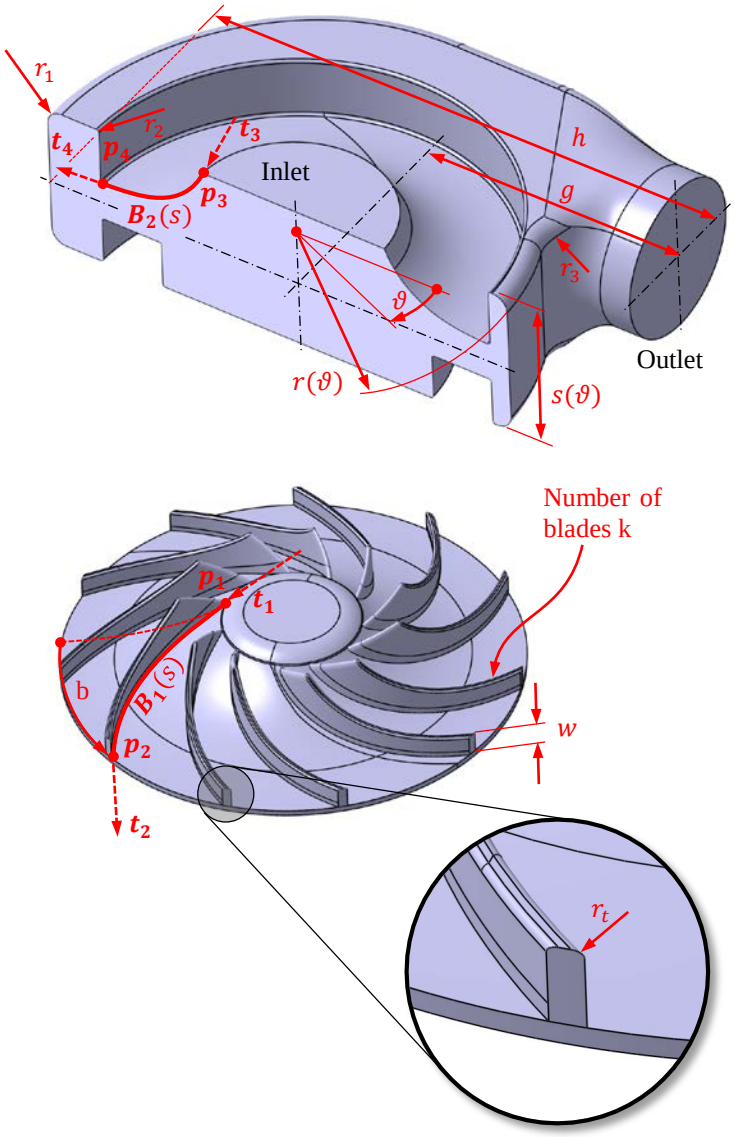

Fig. 1: Parametric model of the housing (section view, above) and the rotor (below). The parametrization of the blade tip geometry is shown in the inset below.

b	angular difference between blade in- and outlet
g	offset between axis and outlet
k	number of blades
$\boldsymbol{p_i}, i = 1 \dots 4$	vertices of the Bézier splines describing the meridional section of the blade
r_1	outer fillet radius of the volute
r_2	inner fillet radius of the volute
r_3	tongue radius
r_t	radius of the blade tip
R	initial radius of the volute (see Eq. (1))
$\boldsymbol{t_i}, i = 2 \dots 4$	tangents of the Bézier splines describing the meridional section of the blade
$s(\vartheta)$	axial depth of the volute
w	axial depth of the blade at outlet
α	slope of the logarithmic spiral (see Eq. (1))

Table 2: Summary of parameters, which govern the design space. Note, that $\boldsymbol{t_1}$ is excluded from the design space, since it is defined by the inlet flow conditions.

OPTIMIZATION ALGORITHM

Considering the large set of parameters (see Table 2), it becomes clear, that a human designer may not easily find the optimal configuration for this aerodynamic device. However, the design process can be largely improved by using modern optimization techniques. For the present case, we use an evolutionary algorithm. It delivers the set of optimal configurations along the Pareto front, from which the designers can choose according to their preference.

The key question is to identify characteristics which contribute to the optimal design. In the present case we aim to

- minimize aeroacoustic noise,
- maximize aerodynamic efficiency, and
- minimize geometric dimensions.

In addition, we require the performance curve of the fan to possess a certain characteristic. The associated objective functions and constraint conditions are outlined in the following subsections.

Objective 1: Aeroacoustic noise. We are interested in the sound pressure level at a distance of 1 m away from the fan. Since the fan is small (diameter 46 mm), it would be very inefficient to directly propagate the sound waves into the far field (which would require to discretize a spherical region of radius 1 m). Instead, we utilize the FW-H equation [17] to perform far field prediction of sound pressure levels. The objective function is formulated as

$$q_1 = \min(L_P) \tag{2}$$

where L_P represents the emitted sound pressure level at a coaxial distance of 1 m away from the fan inlet.

Objective 2: Aerodynamic efficiency. The objective function to maximize the aerodynamic efficiency at the design point is given as

$$q_2 = \max\left(\frac{\Delta p_{\text{stat}} \cdot \dot{V}}{M \cdot \omega}\right) \tag{3}$$

where Δp_{stat} is the static pressure difference between inlet and outlet, $\dot{V}$ is the flowrate, M is the axial moment applied to the rotor and ω is its angular velocity.

Objective 3: Geometric dimensions. To reduce the geometric dimensions of the design, we aim to minimize the overall dimension h of the fan (see Fig. 1)

$$q_3 = \min(h). \tag{4}$$

Constraint condition: Shape of the performance curve. We require the performance curve to possess a strictly negative slope (see Fig. 7). This strategy helps to implicitly measure the flow rate via a pressure sensor (and thereby eliminate costs for an additional sensor in the final product). This requirement is specified as a constraint condition

$$\frac{\partial \psi}{\partial \varphi} < 0 \tag{5}$$

with the non-dimensional flow rate φ and pressure ψ [16] defined in the nomenclature at the end of the paper.

Differential evolution. Evolution algorithms (EA) have been proposed in the seminal papers [18] and [19]. Based on Darwinian evolution, a population of individuals evolve over a search space and adapt to the environment by the use of different strategies such as selection, mutation and crossover. The fitness of individuals increases their chance to survive and get reproduced.

In regard to design optimization problems, EAs exhibit a number of advantages over traditional gradient based methods:

- the objective function does not need to be continuous,
- insensitivity to noise of the objective function (i.e. global minima will be found in the presence of local minima),
- easily adaptable to parallel computing platforms.

However, EAs involve a large number of function evaluations which may be considered as a disadvantage.

Differential Evolution (DE) represents an evolutionary method that was developed more recently. Like all EAs, it is based on populations which are made up of individuals, each of them described by a design vector $\boldsymbol{x}_t = (x_1, x_2, \dots, x_m)$ for generation t, containing m parameters. During each generation, the complete population of design vectors must be evaluated.

For the evolution of design vector $\boldsymbol{x}_t$, the processes of mutation, recombination and selection are performed successively:

Mutation is performed by randomly choosing three unique parameter vectors $\boldsymbol{a}_t, \boldsymbol{b}_t$ and $\boldsymbol{c}_t$ according to $\boldsymbol{a}_t \neq \boldsymbol{b}_t \neq \boldsymbol{c}_t \neq \boldsymbol{x}_t$ to form the new trial vector

$$\boldsymbol{y}_t = \boldsymbol{a}_t + F \cdot (\boldsymbol{b}_t - \boldsymbol{c}_t) \quad (6)$$

Thereby, $F \in]0,2[$ is a user specified constant which controls the amplification of the differential variation $(\boldsymbol{b}_t - \boldsymbol{c}_t)$.

Recombination is the breaking and rejoining of DNA strands to encode novel sets of genetic information. Mathematically, it may be represented by definition of the candidate vector $\boldsymbol{z}_t$

$$z_i = \begin{cases} y_i & \text{if} \quad r_i \leq C \\ x_i & \text{if} \quad r_i > C \end{cases} \quad i = 1 \dots m \quad (7)$$

where r_i is a uniformly distributed random variable $(0 \leq r_i < 1)$ and $C \in]0,1[$ represents a user defined constant.

Finally, the selection process helps to minimize the objective function $f(\boldsymbol{x}_t)$ according to

$$x_{t+1} = \begin{cases} \boldsymbol{z} & \text{if} \quad f(\boldsymbol{z}) \leq f(\boldsymbol{x}_t) \\ \boldsymbol{x}_t & \text{if} \quad f(\boldsymbol{z}) > f(\boldsymbol{x}_t) \end{cases} \quad (8)$$

The methods described above refer to single-objective differential evolution. However, in the context of fan optimization, we require the simultaneous optimization of more than one objective (e.g. aerodynamic efficiency, noise emission and geometric size). Hence, the concepts described above must be extended to multi-objective differential evolution. This was first introduced in [20] by restricting the selection of the individuals $\boldsymbol{a}_t, \boldsymbol{b}_t$ and $\boldsymbol{c}_t$ to the non-dominated individuals. Hence, $\boldsymbol{a}_t \neq \boldsymbol{b}_t \neq \boldsymbol{c}_t$ are required to belong to the Pareto front.

Another approach was described in [21] and [22]: for each generation, all newly created individuals generated by mutation and recombination are added to the population. Hence, the resulting population is twice as large and is subjected to a non-dominated ranking procedure. It selects all non-dominated individuals, gives them the rank 1 and removes them from the population. Successively, the ranking procedure is repeated to identify individuals of higher ranks until the whole population is ranked. In a final step, the original size of the population is obtained by adding individuals from ranks of increasing number, starting from rank 1. These strategies form the core of NSGA-II [22] which has been implemented for the present workflow (see [14] and [15]).

For the inclusion of constraint Eq. (4) we modify the definition of *dominance*. It uses a binary tournament selection, where two solutions are picked from the population and the better solution is chosen. In the presence of constraints, each solution may be either feasible or infeasible. To integrate the constraint into the definition of *dominance*, we propose the following alternative definition for Eq. (8): a solution $\boldsymbol{z}$ is said to constrained-dominate solution $\boldsymbol{x_t}$, if any of the following conditions is true:

1. $\boldsymbol{z}$ is feasible and $\boldsymbol{x_t}$ is not
2. $\boldsymbol{z}$ and $\boldsymbol{x_t}$ is infeasible, but $\boldsymbol{z}$ has a smaller constraint violation
3. $\boldsymbol{z}$ and $\boldsymbol{x_t}$ is feasible and $\boldsymbol{z}$ dominates $\boldsymbol{x_t}$

To take advantage auf automatic parallelization, the algorithm was implemented in a high-level computer algebra system [23].

SIMULATION MODELS

The optimization involves objective functions for (a) aerodynamic and (b) aeroacoustic properties. For their evaluation we are using two different numerical models. These are outlined in the following subsections.

Aerodynamics. The evaluation of the flow field is required for two purposes: (1) to assess the aerodynamic efficiency and (2) to initialize the transient flow field of the aeroacoustic analysis (see below). A stationary RANS solver is sufficient for this purpose [24]. However, the turbulence model requires further consideration, since there are several regions where flow separation is expected. The standard k-ε-model is unable to accurately represent these phenomena. For the present application it has shown to produce results with an error up to 30%. The k-ω-model [25], instead, performs significantly better under adverse pressure gradient conditions. It does not apply damping functions and has straightforward Dirichlet boundary conditions, which leads to significant advantages in numerical stability. In the present study the SST k-ω model was selected [26]. It combines the original Wilcox k-ω model for use near walls and the standard k-ε model away from walls using a blending function. In addition, the eddy viscosity formulation is modified to account for the transport effects of the principle turbulent shear stress. The associated mesh is shown in Fig. 2. It consists of approximately 1.3 million cells. Wall boundaries are discretized using 20 layers of prismatic cells. To show the accuracy of the numerical model, results are compared to measurements of a physical prototype in Fig. 7.

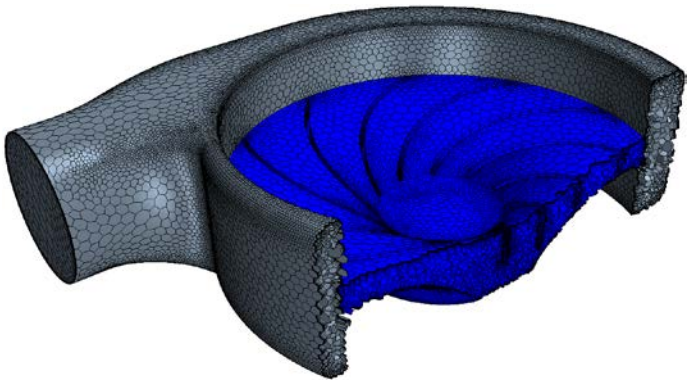

Fig. 2: Discretization of the numerical model for the RANS simulation (section).

Aeroacoustics. For a reliable and unbiased aeroacoustic prediction of flow phenomena, a Large Eddy Simulation (LES) is required. This method is numerically more expensive than a standard Reynolds Averaged Navier-Stokes (RANS) simulation. Various alternative aeroacoustic prediction methods were discussed, for example, in [27]. However, none of them comes close to the fidelity of LES. In the present study, a meshless particle-based kinetic Lattice-Boltzmann solver [28] was chosen for this task. It has a number of advantages:

- It can efficiently perform adaptive wake refinement to trace vortices accurately. This enhances numerical performance by refining the mesh only within areas of large velocity gradients.
- The aeroacoustic simulation requires a higher mesh density than the aerodynamic simulation. Hence, for reasonable simulation times, an efficient parallelization of the numerical algorithm is required. Due to the nature of the LBM, it achieves a superior level of parallel efficiency when compared to traditional mesh based LES methods.

Each simulation was initialized by the steady RANS solution. To obtain a good statistical sample for subsequent digital signal processing of noise data, 80 rotations of the fan were simulated. The correct choice of time step size is governed by the following criteria:

- Convective Courant number: to guarantee stability, it should be below 1.0.
- Maximum resolvable frequency: at least 5 – 10 time steps per oscillation are mandatory for a reliable representation.

In order to comply with the most restrictive of the above mentioned criteria, the time step was set to $\Delta t = 2.5 \cdot 10^{-5}$ s. With this setting, oscillations are correctly represented up to frequencies of around 8000 Hz according to the second criterion.

FW-H SOLVER FOR THE LATTICE BOLTZMANN METHOD

For the optimization we require the sound pressure in the far-field (around 1 m away from the fan). However, it would be very inefficient to discretize the spherical region with radius 1 m around the fan. In order to reduce the numerical cost, the discretization encompasses only the fan and the housing, not the domain surrounding it. The acoustic radiation into the far field has been modeled with the FW-H equation [29]. It represents an exact rearrangement of the continuity equation into the form of an inhomogeneous wave equation. The model is based on the free-space Green's function to compute the sound pressure at the observer location $\bar{x}$. In particular, we use the Farassat Formulation 1A for the non-convective form of the FW-H. Implementation strategies for the FW-H equation using finite-volume discretizations of the URANS method have been published widely. However, for the LBM, alternative algorithmic methods need to be considered. In a similar strategy to the one presented in [30], subsequently we present the steps to apply the FW-H to LBM based solutions.

The time dependent pressure $p'(\bar{\mathbf{x}}, t)$ that is radiated into the surrounding medium at rest is given by

$$p'(\bar{\mathbf{x}}, t) = p'_{\mathrm{T}}(\bar{\mathbf{x}}, t) + p'_{\mathrm{L}}(\bar{\mathbf{x}}, t) + p'_{\mathrm{Q}}(\bar{\mathbf{x}}, t) \qquad (9)$$

Therein, $p'_T(\bar{x}, t)$ is the monopole term, $p'_L(\bar{x}, t)$ is the dipole term and $p'_Q(\bar{x}, t)$ is the quadrupole monopole term. These are given by

$$p'_{\mathrm{T}}(\bar{\mathbf{x}}, t) = \frac{1}{4\pi}\left(-\frac{\partial}{\partial t}\right)\int_S \frac{Q}{r(1-M_{\mathrm{r}})}\,dS \qquad (10)$$

$$p'_{\mathrm{L}}(\bar{\mathbf{x}}, t) = \frac{1}{4\pi}\left(-\frac{\partial}{\partial x_i}\right)\int_S \frac{L_i}{r(1-M_{\mathrm{r}})}\,dS \qquad (11)$$

$$p'_{\mathrm{T}}(\bar{\mathbf{x}}, t) = \frac{1}{4\pi}\left(-\frac{\partial^2}{\partial x_i \partial x_j}\right)\int_V \frac{T_{ij}}{r(1-M_{\mathrm{r}})}\,dV \qquad (12)$$

with $Q = \rho_0 U_i n_i$, $U_i = \left(1 - \frac{\rho}{\rho_0}\right) v_i + \rho u_i/\rho_0$, $L_i = P_{ij} n_i + \rho u_i (u_n - v_n)$, $P_{ij} = (p - p_0)\delta_{ij} - \sigma_{ij}$, $T_{ij} = \rho u_i u_j + \delta_{ij}[(p - p_0) - c_0^2(\rho - \rho_0)] - \sigma_{ij}$. Thereby, u_i is the *i*-th component of the fluid velocity vector and u_n is the fluid velocity component normal to the surface. Accordingly, v_i is the *i*-th component of the surface velocity and v_n is the surface velocity component normal to the surface. Furthermore, n_i is the surface normal vector, σ_{ij} is the viscous stress tensor, ρ_0 is the far field density, P_{ij} is the compressive stress tensor and T_{ij} is the Lighthill stress tensor.

Note that all integrals are evaluated at the retarded time according to

$$g = \tau_{\mathrm{ret}} - t + \frac{l}{c_0} = 0 \qquad (13)$$

with the distance between observer and source at the time of emission given by $l = |\bar{\mathbf{x}} - \bar{\mathbf{y}}(\tau_{\mathrm{ret}})|$.

Note that this model does not include effects such as sound reflections or refractions due to the housing of the fan. This might represent a disadvantage, if we aim to replicate the experimental measurements with the simulation.

Numerical implementation. The FW-H solver requires two inputs: (1) the flow field and (2) the mesh of the integration surface (which is represented by the fan and the interior of the housing for the present application). Both can be imported from the LBM solution. Since the elements of the surface mesh are much smaller than any representative acoustic wave length, they can be considered as compact sources for the FW-H solver. All relevant properties are stored at the center of the surface elements.

For the evaluation of the retarded time equation (see Eq. (13)) we may follow two different strategies: (a) the retarded time algorithm or (b) the source-time dominant algorithm:

Retarded time algorithm. Here the reception time t is fixed, and Eq. (13) is solved for τ_{ret} (i.e. the time of emission of a signal at $\bar{\mathbf{y}}$). Generally, the source position is time-dependent $\bar{\mathbf{y}} = \bar{\mathbf{y}}(\tau_{\mathrm{ret}})$. Hence, Eq. (13) is non-linear and must be solved iteratively. This involves interpolation of the discrete transient input data at time τ_{ret}.

Source-time dominant algorithm. Here the roles of t and τ_{ret} are exchanged, that is the emission time τ is fixed and Eq. (13) is solved for the reception time t. If the observer is stationary, Eq. (13) can be solved analytically.

Although the second approach may seem more attractive, it becomes difficult to manage with large sets of data. Hence, we

have chosen to implement the *retarded time algorithm*. It has the advantage that the integrands in Eqs. (10)—(12) can be evaluated at the time at which the CFD input is available (without time interpolation of input data). Thereby, the FW-H solver will load and operate only on one snapshot of the transient flow field.

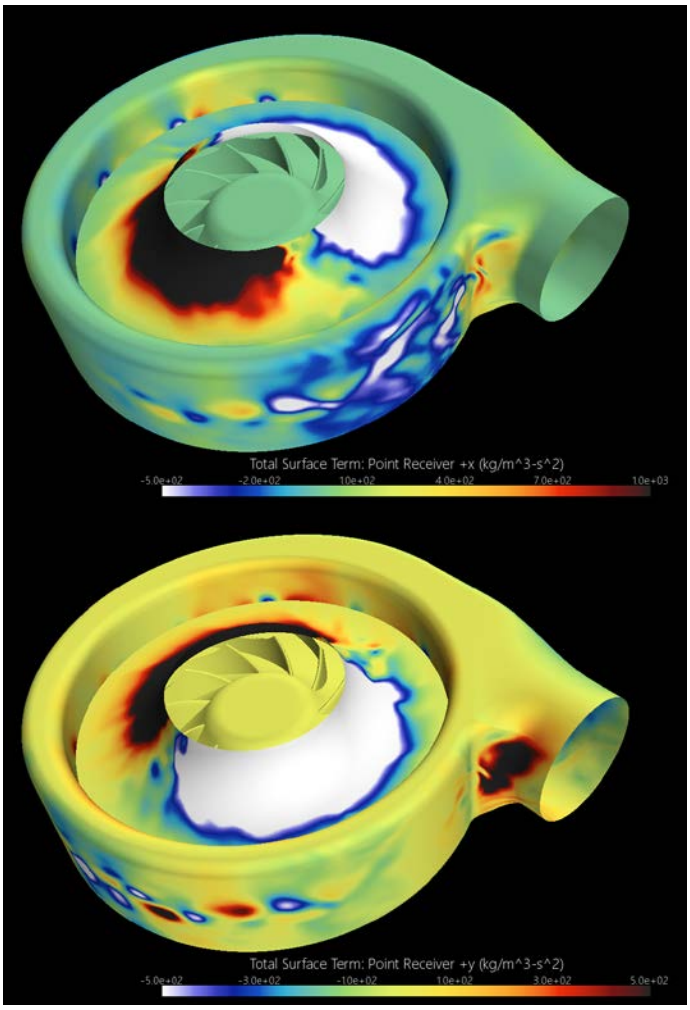

Fig. 3: Monopole and dipole source terms for the Ffowcs Williams-Hawkings model, which are associated with a particular receiver along the positive X-axis (above) and along the positive Y-axis (below).

Note that also for the chosen *retarded time algorithm*, there is some interpolation required for the output pressure time history at the observer. That is because the emission time τ is uniform for all surface elements, but the reception time t is not (due to varying distance between the emitting surface element and the observer). Hence, to rebuild $p'(\bar{\mathbf{x}}, t)$ (see Eq. (9)) we perform piecewise polynomial interpolation. For simplicity, the sampling frequency of the output acoustic pressure signal is the same as the input sampling frequency.

To take advantage of adaptive numerical integration, sophisticated polynomial interpolation and automatic parallelization, the algorithm was implemented using a computer algebra system [23]. The quadrupole term (see Eq. (12)) was omitted, since its contribution was negligible in several tests, which were carried out before the optimization. The source term contributions for two different observers are illustrated in Fig. 3. Obviously, the extrema appear in regions (a) near the tip vortex and (b) at the tongue. The algorithm was validated using a full discretization of the model which includes the observer.

EXPERIMENTAL SETUP

Aerodynamic performances were measured for selected geometries on a suction side throttled facility. The facility is depicted in Fig. 4. Depending on the operating conditions, a pipe is selected, containing an ISO5167 orifice plate for volume flow measurements. The flow then passes through a throttle and a fan, before entering the plenum. In the plenum, flow straighteners and a grid ensure a homogenous, low-turbulent flow. Fan performances are then assessed by means of static pressure difference between the plenum and the measurement room (atmospheric pressure). Since the laboratory is located at nearly 900 m above sea level, a correction is brought in to account for density effects. The test rig is fully ISO5801 compliant.

The aeroacoustic measurements require a more advanced setup. Since the fan motor also emits noise, separating the motor and aerodynamic noise is quite challenging. As a first attempt, acoustic measurements were carried out using two different setups. The first setup consists of a box housing a large silencer and a throttle. The fan is mounted in the box in such a way that only the motor side is freely radiating, whereas fan inflow and outflow sections are mounted in the box. In a second step, the fan is positioned on a damping table, and the outflow pipe is equipped with sound damping material. In both cases, the operating point is controlled by adjusting the throttle and the rotation speed. The sound pressure level is measured at one meter above the fan. The two setups are illustrated in Fig. 6.

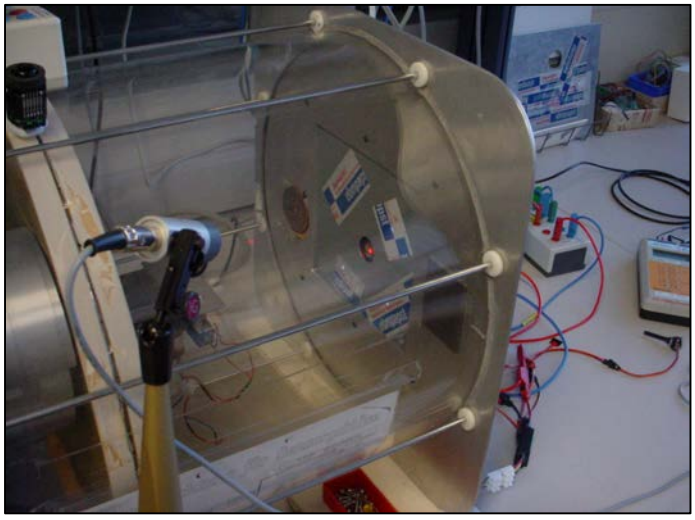

Fig. 4: Aerodynamic test rig.

Fig. 5: Aeroacoustic test rig.

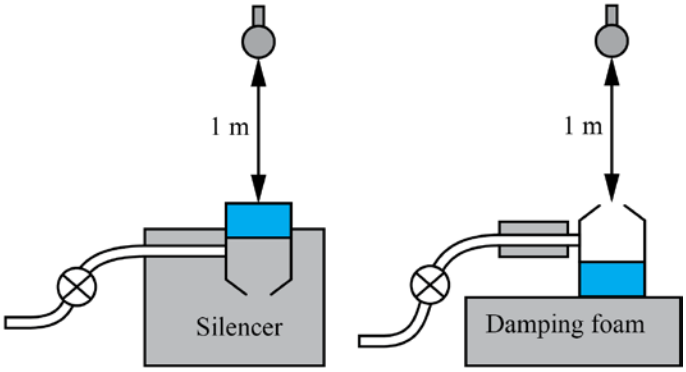

Fig. 6: Two setups for aeroacoustic measurements (blue box = motor).

RESULTS

We begin by studying the improvement of the design due to the optimization. Subsequently, the accuracy of the numerical model is evaluated. The performance of the optimization algorithm is illustrated by showing the Pareto front. In order to understand the involved noise generation phenomena, we perform a study of the dominant vortex structures. Finally, a sensitivity study is performed, evaluating the impact of selected design parameters towards the objective function q_1 and q_2.

Improvement due to the optimization. The initial design had three disadvantages: (1) high level of noise emission, (2) large amount of power consumption (i.e. low aerodynamic efficiency) and (3) undesirable characteristic of the performance curve (we desire a strictly negative slope of the curve, see Eq. (5)). These disadvantages were removed during the optimization: the sound pressure was reduced by 16.6 dBA and the maximum aerodynamic efficiency was increased from 17% to 55% (see dashed lines in Fig. 7 which were both obtained by measurements using physical prototypes, efficiency of the motor: 49%). The most important geometric parameters, which are responsible for this change are (in decreasing order of impact): (1) initial radius of the volute R, (2) tongue radius r_3, (3) fillet radius at the blade tip r_t, (4) axial depth of the volute $s(\vartheta)$, (5) blade geometry (governed by the tangents $\mathbf{t}_i, i = 1 \dots 4$) and (6) axial depth of the blade at the outlet w.

Note that, according to constraint Eq. (5), the characteristic of the performance curve was changed. The initial design shows a peak which was undesirable for the present application (see Fig. 7, solid blue line and red arrow). In contrast, the final design possesses the desired strictly negative slope (see solid black line, Fig. 7).

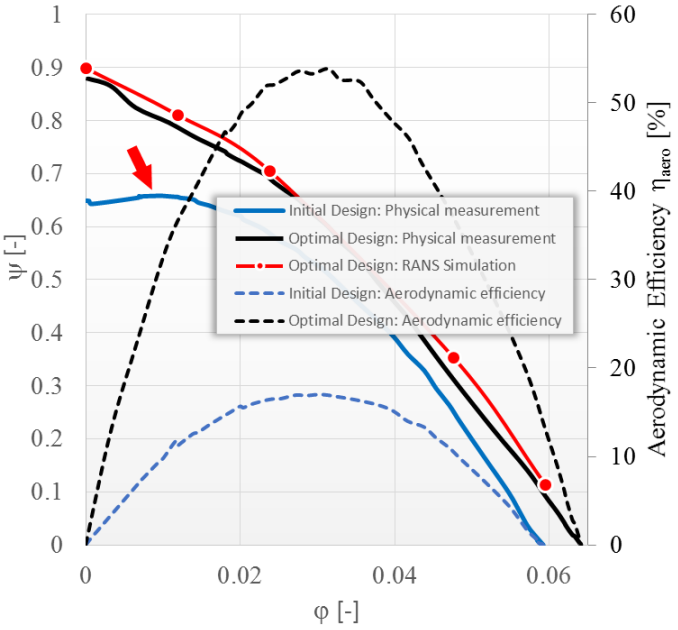

Fig. 7: The improvement due to the optimization is illustrated by comparing the aerodynamic efficiency (see Eq. (3)) for initial design (dashed blue line) and final design (dashed black line).

Validation of the numerical model. For a successful optimization, the numerical model must be able to accurately replicate measurements of the physical prototype. In order to perform this benchmark analysis, the deviation between simulation and physical measurements is evaluated by comparing the dimensionless performance diagrams (see Fig. 7). Clearly, the numerical model (Fig. 7, solid red line) is able to replicate the physical measurement (Fig. 7, black solid line) down to an error of around 3 % across the whole range of operation.

Discussion of the Pareto front. To study the evolutionary progress throughout the optimization procedure, we show the objective space with generations G5 – G20 in distinct colors (see Fig. 9). The Pareto front represents the collection of physically best possible individuals, which spans a 3D surface. It is shown in Fig. 9 by a set of contours (black dashed lines) for constant values of objective function q_3 (see Eq. (5) and Fig. 1). The parameters for the final design for the product were chosen on contour $q_3: h = 62.5$ mm (see Fig. 9, white star).

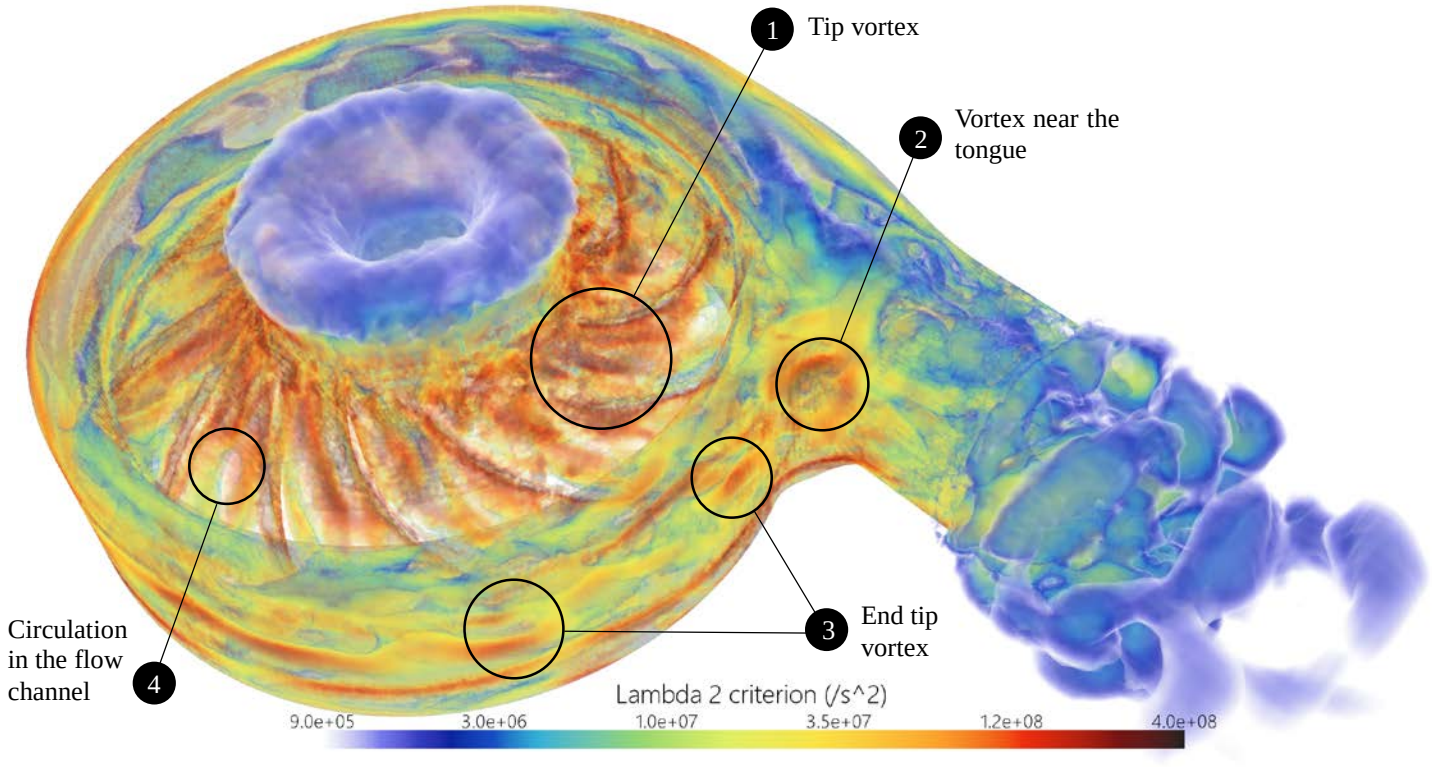

Fig. 8: Visualization of the vortex structure. The λ_2 criterion illustrates the location of high-energy flow structures (large eddy simulation of the fan).

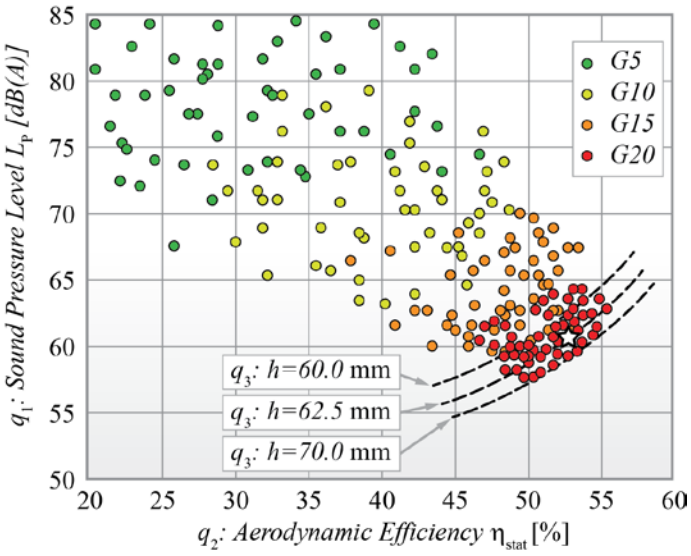

Fig. 9: Objective space for the optimization showing the evolution of the population. The generations G5 – G20 are displayed in distinct colors. The Pareto front is illustrated by contours (black dashed lines). The optimum candidate, which was chosen for the final product, is indicated by a white star.

Analysis of dominant vortex structures. In order to understand sound production mechanisms within the fan assembly, it may be useful to study the dominant vortex structures. For the identification of these structures, the vorticity $\omega = |\nabla \times \mathbf{u}|$ alone is not suitable since it cannot distinguish between pure shearing motions and the actual swirling motion of a vortex [31]. This property would lead to a misrepresentation of the vortex geometry. Instead the λ_2 criterion is preferred. It is based on the decomposition of the velocity gradient tensor $\mathbf{J}$ into its symmetric part (the rate of deformation or strain-tensor $\mathbf{S}$) and its antisymmetric part (the spin tensor $\mathbf{\Omega}$) according to

$$\mathbf{S} = \frac{\mathbf{J} + \mathbf{J}^T}{2} \qquad \mathbf{\Omega} = \frac{\mathbf{J} - \mathbf{J}^T}{2} \tag{14}$$

A vortex is then defined as a connected region where $\mathbf{S}^2 + \mathbf{\Omega}^2$ has two negative eigenvalues. Because $\mathbf{S}^2 + \mathbf{\Omega}^2$ is real and symmetric, it has only real eigenvalues. Let λ_1, λ_2 and λ_3 be the eigenvalues such that $\lambda_1 \geq \lambda_2 \geq \lambda_3$. If λ_2 is negative at a point, then that point belongs to a vortex core.

The study of vortex structures for the present fan assembly reveals several zones of interest (see Fig. 8). These findings may be used to reconsider the design space (i.e. include additional parameters to perform further optimization) or to better understand the effects observed in the sensitivity study performed subsequently.

SENSITIVITY OF SELECTED DESIGN PARAMETERS

The simulation framework conveniently allows to perform sensitivity studies. Thereby we analyze the change of

- emitted sound pressure (objective q_1, see Eq. (2)), and
- the aerodynamic efficiency (objective q_2, see Eq. (3))

as a function of certain geometric parameters. This is useful to extract reusable design knowledge for future developments.

We will study the geometric features, which are associated with the dominant vortex structures identified in the previous subsection. In particular, we focus on the flow phenomena and associated geometric features listed in Table 3. For each parametric modification, the optimized geometry is chosen as a reference. To illustrate the procedure, it is demonstrated in detail for the blade tip radius r_t subsequently.

Geometric parameter	Associated flow phenomenon
Blade tip radius r_t	Tip vortex
Tongue radius r_3	Flow separation near tongue
Initial radius of volute R	Separation of high- and low-pressure part of volute, tip vortex at the end of the blade
Number of blades k	Frequency of pulsatile pressure near tongue

Table 3: Geometric parameters (see Fig. 1), whose sensitivities are studied subsequently. The associated flow phenomena are noted.

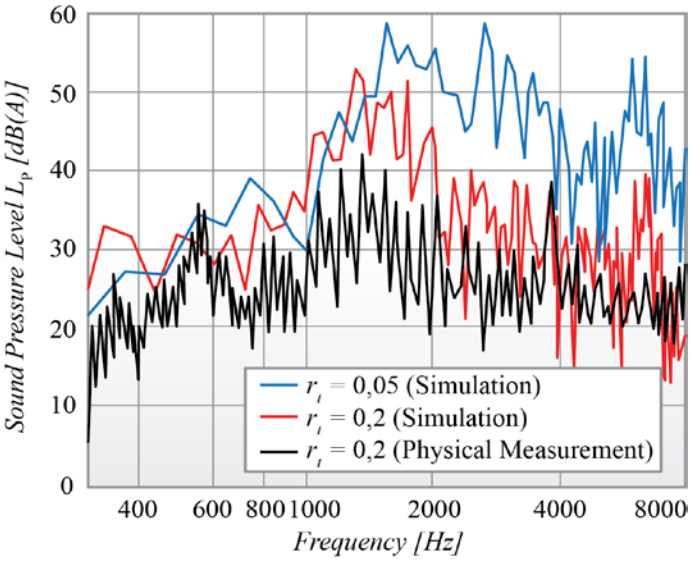

Fig. 10: Frequency spectra of the emitted sound pressure for two different configurations of the blade tip radius: r_{t1} = 0.2 mm (red curve) and r_{t2} = 0.05 mm (blue curve). The first configuration is compared to a physical measurement (black curve). The sound pressure is evaluated at a coaxial distance of 1 m away from the fan inlet.

Sensitivity of the blade tip radius r_t. We analyze the sound pressure frequency spectra for two different geometric configurations: r_{t1} = 0.2 mm and r_{t2} = 0.05 mm, see Fig. 10. The acoustic observer is located at a coaxial distance of 1 m away from the fan inlet. The total sound pressure difference between these two configurations is 7,9 dBA. For the first configuration we also show the experimental results (see black curve in Fig. 10). The peak at around 600 Hz is attributed to imbalance of the rotor.

For increasing values of r_t, the sound pressure L_p is decreasing monotonously (larger values of r_t are causing lower energy flow separation vortices at the blade tip, see vortex 1, Fig. 8). However, also the aerodynamic efficiency is decreasing due to increased gap losses. The sensitivity diagram for r_t is shown in Fig. 11.

Note, that since the rotor is a small object (diameter 46 mm), the analyzed geometric features may not be accurately reproduced using rapid prototyping. In particular, the fillet radius r_t under investigation may suffer from the limited resolution of the rapid prototyping process. Hence, the sensitivity of sound pressure with respect to the selected parameters may only reasonably be studied within a simulation framework – not with a physical prototype created by rapid prototyping. However, the final product will be manufactured by an injection die molding process, which does not suffer from limited resolution.

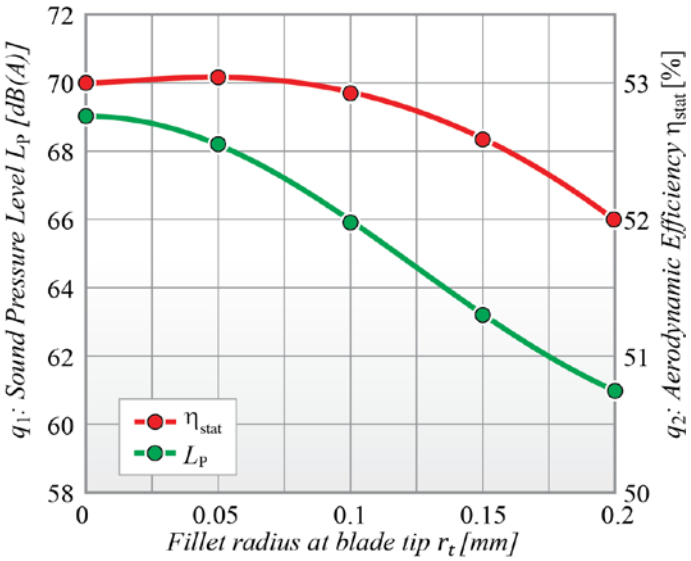

Fig. 11: Sensitivity of design parameter r_t (fillet radius at blade tip).

Sensitivity of the tongue radius r_3. For small values of the tongue radius, the tongue forms a concave part of the housing. This helps to reduce flow separation at the outlet of the fan, thereby increasing aerodynamic efficiency and reducing the emitted sound pressure. However, for increasing values of r_3, there are two effects causing increased noise emission and reduced aerodynamic efficiency:

- flow separation at the tongue (see vortex 2, Fig. 8), and
- shortened effective angular path length of the volute to accumulate pressure.

Note that small values of r_3 require large values of g (offset between rotor axis and outlet, see Fig. 1). In the present study, the minimization of g was important. Hence, this constrained the choice of r_3. The sensitivity diagram for the tongue radius r_3 is shown in Fig. 12.

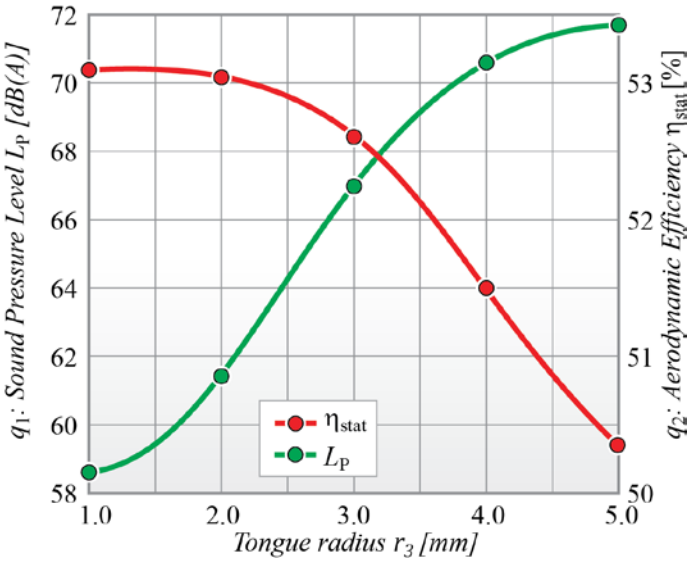

Fig. 12: Sensitivity of design parameter r_3 (tongue radius).

Sensitivity of initial radius of the volute *R*. For small values of R, there is better separation between the high- and the low-pressure part of the volute (reduced adverse flow at the tongue). This increases the aerodynamic efficiency. However, with these configurations, there is only a small distance between rotor outlet and volute wall. Hence, the pressure difference between suction side and pressure side of the blade causes high energy tip vortices at the outer radius of the blade (see vortex 3, Fig. 8). This leads to an increased emission of noise.

For larger values of R, the intensity of both flow phenomena discussed above is decreased. This reduces the aerodynamic efficiency and the emitted sound pressure (see Fig. 13).

Sensitivity of the number of blades *k*. For a small number of blades k there are aerodynamic losses due to recirculation in the flow channel. However, for a large number of blades k, the losses due to friction at the blade walls are increasing. Hence, the maximum aerodynamic efficiency can be observed for a number of $k = 9$ blades (see Fig. 14).

When considering the emission of noise as a function of k, there are two mechanisms involved:

1. The frequency of tonal noise depends on the number of blades. The A-weighting filter emphasizes frequencies above 3 kHz where the human ear is most sensitive, while attenuating lower frequencies. Hence, the larger number of blades causes larger values of emitted sound pressure.
2. In addition, for each blade there is flow separation at the tip (see vortex 1, Fig. 8). A larger number of blades k means there are more vortices involved in the accumulation of noise emission.

The minimum for the emitted sound pressure can be observed for a number of $k = 7$ blades. For a smaller number of blades, there is recirculation in the flow channel (see vortex 4, Fig. 8) which seems to contribute to increased noise emission. The sensitivity diagram for the number of blades k is shown in Fig. 14.

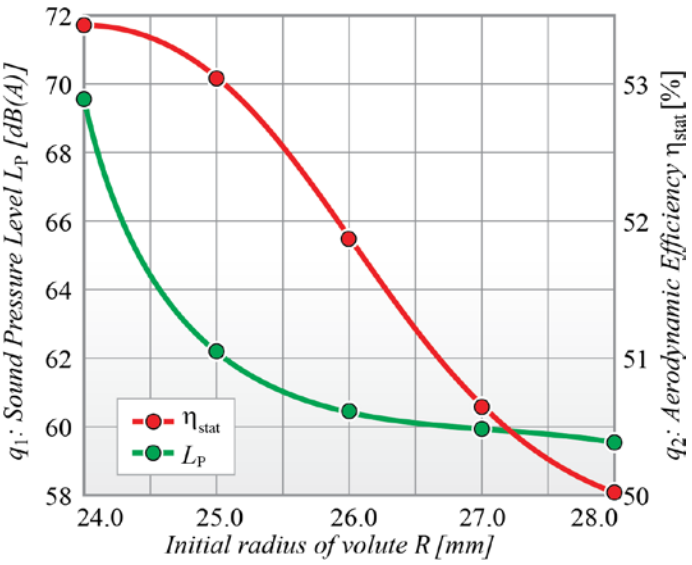

Fig. 13: Sensitivity of design parameter R (initial radius of volute).

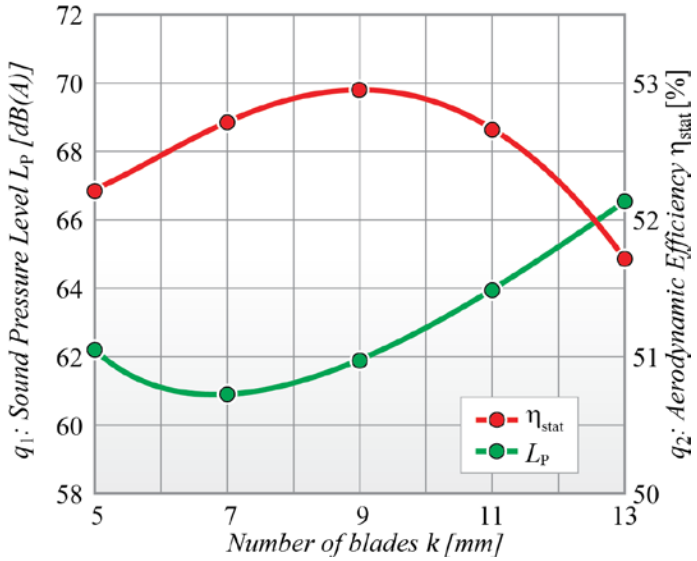

Fig. 14: Sensitivity of design parameter k (number of blades).

CONCLUSION

BPAP devices are used widely in clinical applications. However, their main disadvantage is patient related non-compliance due to (a) bulkiness and (b) noise emission.

We have described a multi objective optimization framework to tackle both problems. It operates on a parametric model of the fan and housing (see Fig. 1). The optimization problem is described using three objective functions (see Eqs. (2) –(4). They are evaluated using a RANS solver (for the aerodynamic efficiency) and a Lattice Boltzmann (LBM) based code (for the aeroacoustics). For the far-field propagation of

sound waves, we presented efficient implementation strategies for the FW-H equation to be used with the LBM.

In addition to the optimization objectives, we specified a constraint condition with respect to the characteristic of the performance diagram (strictly negative slope, see Eq. (5)). This strategy helps to reduce costs for sensors in the final product.

The optimization is driven by an NSGA-II evolution algorithm. It conveniently evaluates the Pareto front of best possible solutions. From these solutions, the designer may then choose according to the projected requirements.

To understand the noise production mechanisms, we analyzed the vortex structure (see Fig. 8). For the geometric features, which are associated with the dominant vortices, we performed a sensitivity study with respect to their geometric parameters. Some of these features are too small to be replicated reliably with rapid prototyping models. Hence, the simulation is the only way to extract this engineering knowledge, which may be reused for future design projects.

Due to the large number of parameters involved, the design of fans for BPAP devices is complex. Compared to the proposal from a human designer, the newly developed strategy has helped to increase the aerodynamic efficiency by 210% (see Fig. 7), thereby reducing overall geometric size. Furthermore, the design procedure was accelerated considerably.

NOMENCLATURE

$\boldsymbol{a}_\mathbf{t}, \boldsymbol{b}_\mathbf{t}, \boldsymbol{c}_\mathbf{t}$ = parameter vectors (diff. evol.) (–)
b = angular difference between blade inlet and outlet (°)
D = diameter of the fan (m)
g = offset between axis and outlet of the fan (m)
h = overall width of the housing (m)
$\mathbf{J}$ = velocity gradient tensor
k = number of blades (–)
L_P = sound pressure level (dB)
L_W = sound power level (dB)
M = torque of the rotor (Nm)
n = rotational speed of the rotor (s^{-1})
$\boldsymbol{p}_\mathbf{i}$ = vertices of the Bézier spline for the meridional section (m)
p_{stat} = static pressure (Pa)
p_{tot} = total pressure (Pa)
$p'(\bar{\boldsymbol{x}}, t)$ = time dependent pressure (Pa)
q_i = objective function (dB, –)
$r(\vartheta)$ = radius of the volute (m)
r_1 = outer fillet radius of volute (m)
r_2 = inner fillet radius of volute (m)
r_3 = tongue radius (m)
r_t = radius of blade tip (m)
R = initial radius of the volute (m)
$s(\vartheta)$ = axial depth of the volute (m)
$\mathbf{S}$ = strain-tensor
t = reception time (FW-H solver) (s)
$\boldsymbol{t}_\mathbf{i}$ = tangent of the Bézier spline for the meridional section (m)
$\dot{V}$ = flow rate (m^3/s)
w = axial depth of blade at outlet (m)
$\bar{\mathbf{x}}$ = location of acoustic observer (m)
$\boldsymbol{x}_\mathbf{t}$ = design vector (diff. evol.) (–)
$\bar{\mathbf{y}}$ = location of acoustic source (m)
$\boldsymbol{y}_\mathbf{t}$ = trial vector (diff. evol.) (–)
$\boldsymbol{z}_\mathbf{t}$ = candidate vector (diff. evol.) (–)

α = slope of logarithmic spiral for volute (–)
ϑ = angular coordinate (fan axis) (rad)
λ_i = eigenvalue of the strain tensor (–)
ρ = density of air (kg/m^3)
τ = Emission time (FW-H solver) (s)
$\varphi = 4\dot{V}/(\pi^2 D^3 n)$ = dimensionless flow rate (–)
$\psi = 2\Delta p_{\mathrm{tot}}/(\pi^2 \rho D^2 n^2)$ = dimensionless pressure (–)
ω = angular velocity of the rotor (s^{-1})
$\boldsymbol{\Omega}$ = spin tensor (s^{-1})

ACKNOWLEDGMENTS

The authors would like to thank G. Eimer and B. Graf for performing the experiments. In addition, the authors would like to thank ebm-papst St. Georgen GmbH, Ninsight and Amazon Inc. for supporting this study.

REFERENCES

[1] J. S. Bradley, C. L. Byington, S. S. Shah, B. Alverson, E. R. Carter, C. Harrison, S. L. Kaplan, S. E. Mace, G. H. McCracken, M. R. Moore, S. D. St Peter, J. A. Stockwell and J. T. Swanson, "The Management of Community-Aquired Pneumonia in Infants and Children Older Than 3 Months of Age: Clinical Practice Guidelines by the Pediatric Infectous Diseases Society and the Infectous Diseases Society of America," Oxford University Press, 2011.

[2] O. S. Levine, K. L. O'Brien, M. Deloria-Knoll, D. R. Murdoch, D. R. Feikin, A. N. DeLuca, A. J. Driscoll, H. C. Baggett, W. A. Brooks, S. R. C. Howie, K. L. Kotloff, S. A. Madhi, S. A. Maloney, S. Sow, D. M. Thea and J. A. Scott, "The Pneumonia Etiology Research for Child Health Project: A 21st Century Childhood Pneumonia Etiology Study," *Pneumonia Etiology Research in Children*, vol. 54, no. 2, pp. 93-101, 2012.

[3] S. F. Sufahani, N. A. Mohd Razali, M. F. Mormin and A. Khamis, "An Analysis of the Prevalence of Pneumonia for Children under 12 Year Old in Tawau General Hospital, Malaysia," in *International Seminar on the Application of Science & Mathematics 2011*, Kuala Lumpur, 2012.

[4] F. W. S. Ko and D. S. C. Hui, "Air pollution and chronic obstructive pulmonary disease," *Respirology*, vol. 17, pp. 395-401, 2012.

[5] J. R. Hurst, J. Vestbo, A. Anzueto, N. Locantore, H. Müllerova, R. Tal-Singer, B. Miller, D. A. Lomas, A. Agusti, W. MacNee, P. Calverley, S. Rennard, E. F. M. Wouters and J. A. Wedzicha, "Susceptibility to Exacerbation in Chronic Obstructive Pulmonary Disease," *N Engl J Med*, pp. 1128-1138, 2010.

[6] L. J. Akinbami, J. E. Moorman, C. Bailey, H. S. Zahran, M. King, C. A. Johnson and X. Liu, "Trends in Asthma Prevalence, Health Care Use, and Mortality in the United States, 2001-2010," U.S. Department of Health and Human Services, 2012.

[7] S. K. Sharma, S. Agrawal, D. Damodaran, V. Sreenivas, T. Kadhiravan, R. Lakshmy, P. Jagia and A. Kumar, "CPAP for the Metabolic Syndrome in Patients with Obstructive Sleep Apnea," *N Engl J Med*, pp. 2277-2286, 2011.

[8] A. D. Rueda, R. Santos-Silva, S. M. Togerio, S. Tufik and L. R. A. Bittencourt, "Improving CPAP Compliance by a Basic Educational Program with Nurse Support for Obstructive Sleep Apnea Syndrome Patients," *Sleep Science*, vol. 2, no. 1, pp. 8-13, 2009.

[9] J. Collen, C. Lettieri, W. Kelly and S. Roop, "Clinical and polysomnographic predictors of short-term continuous positive airway pressure compliance," *Chest*, vol. 135, no. 3, pp. 704-709, 2009.

[10] K. Bamberger, T. Carolus and M. Haas, "Optimization of Low Pressure Axial Fans and Effect of Subsequent Geometrical Modifications," in *Proceedings of Fan Noise*, Lyon, 2015.

[11] S. Magne, M. Sajosé, S. Moreau and A. Berry, "Numerical Optimization of Fan Tonal Noise Control using Acoustic Modulation of Slowly-Rotating Obstructions," in *20th AIAA/CEAS Aeroacoustics Conference, AIAA Aviation*, 2014.

[12] M.-W. Heo, T.-W. Seo and H.-S. Shim, "Advanced Integrated Design Optimization System Using 3D Aerodynamic and Aero-Acoustic Analyses for Design of an Axial Fan," in *Proceedings of Fan Noise*, Lyon, 2015.

[13] M. Stadler, M. Schmitz, P. Ragg, D. Holman and R. Brionnaud, "Aeroacoustic Optimization of Axial Fans with the Lattice-Boltzmann Method," in *ASME Turbo Expo 2012: Turbine Technical Conference and Exposition*, Copenhagen, Denmark, 2012.

[14] M. Stadler, M. Schmitz and W. Laufer, "GPGPU based aeroacoustic optimization of a contra rotating fan," in *ASME Turbo Expo*, Düsseldorf, 2014.

[15] M. Stadler, M. Schmitz, W. Laufer and P. Ragg, "Inverse aeroacoustic design of axial fans using genetic optimization and the Lattice-Boltzmann method," *ASME J. Turbomach.*, vol. 136, no. 4, p. 041011, 2014.

[16] T. Carolus, Ventilatoren, Siegen, Germany: Springer Verlag, 2013.

[17] C. G. Crighton, A. P. Dowling, J. E. Ffowcs Williams, M. A. Heckel and F. A. Leppington, Modern Methods in Analytical Acoustics: Lecture Notes, New York: Springer, 2013.

[18] J. Holland, Adaptation in Natural and Artificial Systems, University of Michigan Press, 1975.

[19] J. Rechenberg, Optimierung technischer Systeme nach Prinzipien der biologischen Evolution, Stuttgart: Frommann-Holzboog, 1973.

[20] H. Abbas, R. Sarker and C. Newton, "PDE: A Pareto-Frontier Differential Evolution Approach for Multi-Objective Optimization Problems," in *Proceedings of the Congress on Evolutionary Computation*, Piscataway, New Jersey, 2001.

[21] N. Madavan, "Multiobjective Optimization using a Pareto Differential Evolution Approach," in *Proceedings of the Congress on Evolutionary Computation*, Honolulu, Hawaii, 2002.

[22] K. Deb, S. Agrawal, A. Pratap and T. Meyarivan, "A fast elitist Non-Dominated Sorting Genetic Algorithm for Multi-Objective Optimization: NSGA-II," in *Proceedings of the Parallel Problem Solving from Nature VI Conference*, Paris, France, 2000.

[23] Wolfram Research Inc., Mathematica User Manual V 10.2, Illionois, USA, 2015.

[24] CD-Adapco, Star-CCM+ User Manual, Melville, New York, 2015.

[25] D. Wilcox, Turbulence Modeling for CFD, D C W Industries, 2006.

[26] T. C. Rebollo and R. Lewandowski, Mathematical and Numerical Foundations of Turbulence Models and Applications, Basel: Birkhäuser, 2014.

[27] H. Reese and T. Carolus, "Axial Fan Noise: Towards Sound Prediction basd on Numerical Unsteady Flow Data - A Case Study," in *Acoustics'08*, Paris, 2008.

[28] Nextlimit Inc., XFlow User Manual, Madrid, 2015.

[29] S. Mendez, M. Shoeybi, K. L. Sanjiva and M. Parviz, "On the use of the Ffowcs Williams-Hawkings equation to predict far-field jet noise from large-eddy simulations," *Int. J. of Aeroacoustics*, vol. 12, no. 1, pp. 1-20, 2013.

[30] G. A. Brès, F. Pérot and D. Freed, "A Ffowcs Williams–Hawkings Solver for Lattice-Boltzmann based Computational Aeroacoustics," in *16th AIAA/CEAS Aeoroacoustics Conference*, Stockholm, 2010.

[31] V. Kolár, "Vortex identification: New requirements and limitations," *Int. J. of Heat and Fluid Flow*, vol. 28, pp. 638-652, 2007.